The Thesis Committee for Kevin Thomas Baar
Certifies that this is the approved version of the following Thesis:

Phosphine-Capped Nanoparticles for Electrocatalysis

APPROVED BY
SUPERVISING COMMITTEE:

Simon M. Humphrey, Supervisor

Richard M. Crooks, Co-supervisor

Phosphine-Capped Nanoparticles for Electrocatalysis

by

Kevin Thomas Baar

Thesis

Presented to the Faculty of the Graduate School of

The University of Texas at Austin

in Partial Fulfillment

of the Requirements

for the Degree of

Master of Arts

The University of Texas at Austin

December 2020

Abstract

Phosphine-Capped Nanoparticles for Electrocatalysis

Kevin Thomas Baar, M.A.

The University of Texas at Austin, 2020

Supervisor: Simon M. Humphrey

Co-Supervisor: Richard M. Crooks

In this work, a new method of synthesizing gold-rhodium alloyed nanoparticles (Au-Rh NPs), stabilized by triphenylphosphine (PPh_3) ligands is reported. This method has only previously been used to synthesize monometallic $Au_{55}(PPh_3)_{12}Cl_6$ (Au55) and $Rh_{55}(PPh_3)_{12}Cl_6$ (Rh55) nanoparticles. The NPs were characterized using transmission electron microscopy (TEM), scanning transmission electron microscopy (STEM), energy dispersive X-ray spectroscopy (EDS), nuclear magnetic resonance (NMR), and time-of-flight secondary ion mass spectrometry (TOF-SIMS). It was observed that the synthesis produced NPs with the same size as Au55 and Rh55 and a wide range of alloy compositions as well as gold nanoparticles (AuNPs) and rhodium nanoparticles (RhNPs). The electrocatalytic activity for the oxygen reduction reaction (ORR) is explored for the Au-Rh NPs and compared with the activities of Au55 and Rh55 using cyclic voltammetry (CV) and rotating ring disk voltammetry (RRDV).

Table of Contents

List of Tables

List of Figures

Chapter 1: Introduction

Today, greenhouse gas emissions are a global problem and gasoline powered vehicles are the third leading source of CO_2 emissions.[1] One promising solution to mitigate greenhouse gas emissions is to implement hydrogen fuel cells into vehicles, which provide a cleaner alternative to fossil fuels by emitting only water. Unfortunately, the oxygen reduction reaction (ORR), which occurs at the fuel cell cathode, requires a large amount of extra energy to be favorable.[2] Additionally, catalysts that efficiently perform the ORR are often precious metals, which are expensive and scarce. One way to tackle this energy barrier is through the design and investigation of new catalysts, such as small (<2 nm) nanoparticles (NPs) with specific capping ligands that can modulate the activity of the catalyst. By varying alloy compositions of these NP catalysts, their electronic properties can be tuned to optimize catalyst performance and amounts of precious metals can be minimized. This work focuses on the synthesis and characterization of AuNPs, RhNPs, and Au-Rh NPs stabilized with PPh_3 capping ligands, which are predicted to show favorable results for the catalysis of ORR.

1.1 Fuel Cells and Oxygen Reduction

Proton exchange membrane fuel cells work by oxidizing a fuel-most commonly hydrogen or methanol-at the anode. In the case of a hydrogen fuel cell, H_2 gas is passed over the anode surface, where it is split into protons at the anode. The resulting protons travel through an electrolyte, to the cathode. Molecular oxygen (O_2) is passed over the cathode surface, where a catalyst uses the protons (generated at the anode) to reduce O_2

into water. The oxidation of the fuel at the anode is very facile with platinum (Pt) catalysts; however, the energy required to break the double bond in O_2 at the cathode is the origin of many of the fuel cell's inefficiencies.[3]

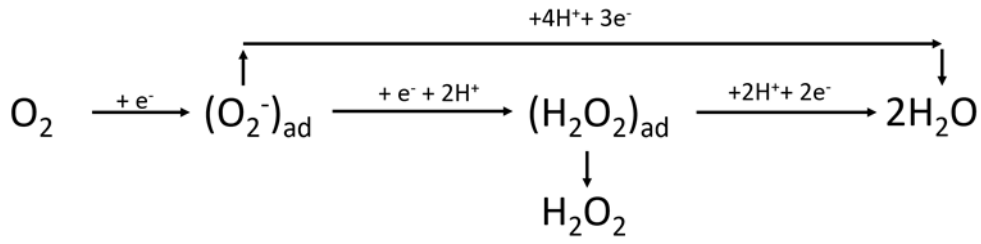

Figure 1.1: Two-electron and four-electron pathways for the ORR.

This inefficiency at the cathode has resulted in a widespread search to find catalysts with lower overpotentials-the difference in standard reduction potential and experimentally observed potential-required to reduce O_2. The standard reduction potential for O_2 is +1.23 V, and the most favored reaction is the four-electron reduction from O_2 to 2 equivalents of H_2O. The other accepted pathway involves two two-electron reductions with a peroxide intermediate. Pt catalysts generally proceed *via* the four-electron reduction. Other catalysts such as gold (Au) based catalysts, reduce O_2 mainly by the two-electron with more H_2O_2 production than Pt.

One proposed mechanism for ORR *via* the four-electron pathway (Figure 1.2) involves binding of an O_2 molecule to the catalyst surface followed by two independent reactions between surface-bound O-O and two protons and two electrons to give 2•H_2O. For many

years, Pt has been considered the state-of-the-art catalyst for use at the cathode to drive ORR.[4] However, Pt catalysts have many drawbacks, including low durability, easy poisoning from trace carbon monoxide in the air (which reduces catalytic activity), and high cost due to low availability.[5] For these reasons, large scale use of Pt in hydrogen fuel cells is not industrially viable. There have been attempts to increase the efficiency of ORR and reduce the amount of Pt by using Pt alloy NPs,[6,7] but the catalytic activity is not high enough for the fuel cell to be cost effective. Additionally, fuel cells can be operated at both alkaline and acidic pH values. Alkaline fuel cells are not practical for automotive applications due to CO_2 impurities present in the atmosphere which lead to precipitation of carbonates at high pH values; these carbonates eventually poison the catalyst. Therefore, these fuel cells operating under basic conditions are mostly used in space.[3] Alternatively, acidic fuel cells are more applicable to the automotive industry; with this application in mind, all of the ORR in this work was done in acidic media.

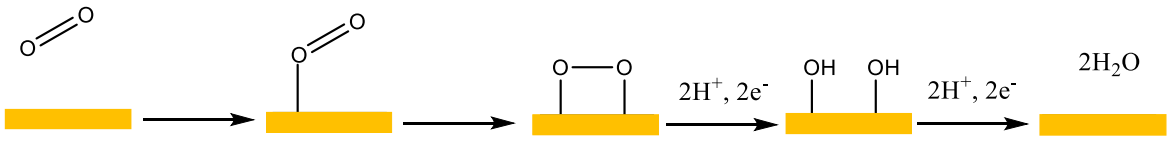

Figure 1.2: One possible mechanism for O_2 binding, dissociation, and reduction on a catalyst surface.

1.2 NANOPARTICLES AS CATALYSTS

In recent years, NPs have been researched and used as catalysts for many different electrocatalytic reactions including carbon monoxide oxidation,[8,9] carbon dioxide reduction,[10,11] methanol oxidation,[12,13] and O_2 reduction,[6,14,15] the latter of which shall be

the focus of this work. Currently, carbon supported Pt catalysts are the most widely used catalyst in hydrogen fuel cells. This is largely because, Pt has the lowest overpotential for ORR in comparison with other transition metals. Numerous studies have been performed to find an ORR catalyst with a lower overpotential and that is more cost effective than Pt for use in large scale production of fuel cells.[7,16,17] ORR with bulk metal catalysts has been extensively studied, both experimentally and theoretically. One significant contribution to the theoretical understanding of the ORR came with the creation of a volcano plot by Nørskov *et al*,[18] which plots the relationship between reactant and product binding energies and catalytic activity (Figure 1.3). Using this information, an ideal catalyst would have both a favorable binding energy for the reactant as well as a weak enough binding energy for the product so it can be released to regenerate the catalyst and complete a catalytic cycle. It is well known from theoretical volcano plots and experimental data that bulk, monometallic Au and rhodium (Rh) are insufficient catalysts for ORR.[19] Bulk Au has proven to be a poor catalyst due to its resistance to oxidation, while Rh's affinity for O_2 is too high to be a good catalyst for ORR. Volcano plots can also be made for active sites that are alloys of two or more metals.[20] Different alloy compositions can be made to tune the catalytic activity for a certain process. Alloys of bulk metals and NPs have been shown to have an increased activity compared to their monometallic counterparts.[21] The increase in catalytic activity of alloys will be discussed in the next chapter.

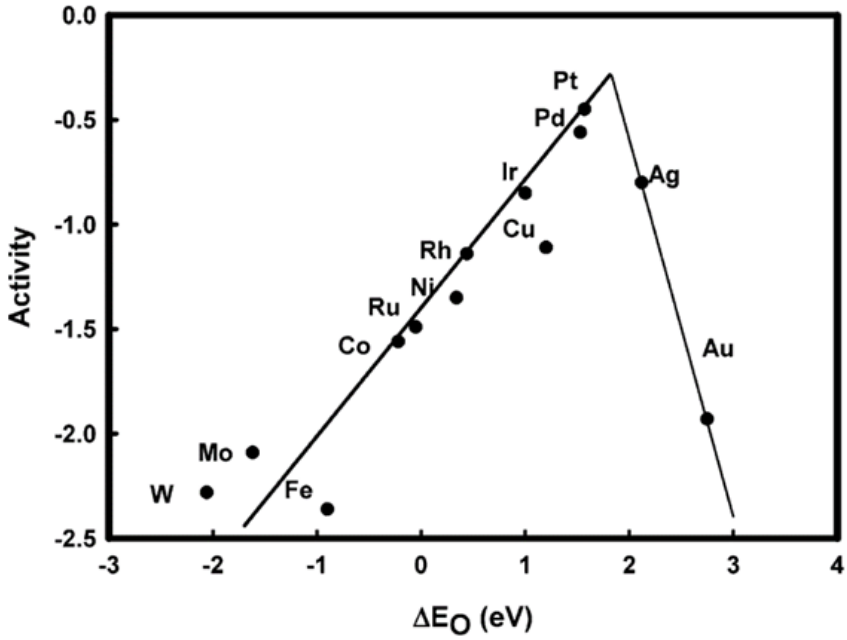

Figure 1.3. Plot of ORR activity vs binding energy of O_2 on bulk metals.[18]

1.3 LIGAND-STABILIZED GOLD NANOPARTICLES

1.3.1 $Au_{55}(PPh_3)_{12}Cl_6$

$Au_{55}(PPh_3)_{12}Cl_6$ (Au55) was first synthesized in 1981 by G. Schmid and co-workers and adopts a two-shell cuboctahedral structure with phosphines on the vertices and Cl atoms in the center of the square (100) faces (Figure 1.4).[22] A shell consists of $10n^2 + 2$ atoms, where n is the shell number; this gives the first, second, and third shells 12, 42, and 92 atoms respectively. Much like noble gases with a complete shell of electrons, NPs with these magic numbers of atoms (13, 55, and 147 total) are more stable than NPs with incomplete outer shells. An X-ray photoelectron spectroscopy study showed that after exposure to an O_2 plasma, Au55 remained Au(0) while AuNPs of different sizes had

oxidized significantly.[23] Au55 is synthesized by the reduction of $AuCl(PPh_3)$ with B_2H_6 at mildly elevated temperature. Due to the relatively complex and hazardous synthesis compared to other NP synthesis methods, the applications of these NPs have not been thoroughly realized. The synthesis of Au55 produces NPs with a diameter of 1.4 nm with high monodispersity. Having a monodisperse sample of NPs is very important for catalysis.

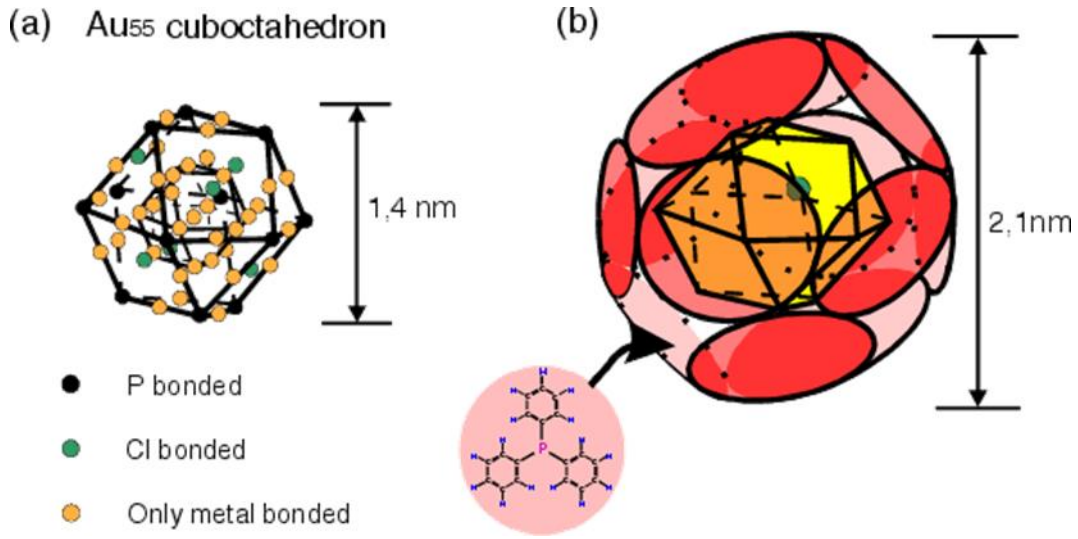

Figure 1.4: (a) Depiction of bonding in Au55 core and (b) PPh_3 ligand shell and their corresponding diameters.[24]

If there is a broad range of NP sizes in a sample, it is not possible to know where the most significant contribution to the catalytic activity comes from. AuNPs are no exception to this. It has been shown that in both alkaline[19,25,26] and acidic[27] electrolytes, catalytic activity is highly dependent on the size of the NPs. These studies showed that as the size of the NPs decreased, the ORR activity of AuNPs increased. This can be attributed in a large part to the fact that the electronic properties of AuNPs significantly change as the size gets further and further from bulk Au.[28]

1.3.2 Other Ligated Gold Nanoparticles

Another potential advantage of these NPs that has not been fully explored is the effect of the phosphine ligands on the NP surface. Organophosphines are thought to sufficiently stabilize the NP core and prevent agglomeration, while remaining open enough for a substrate to reach the surface for catalysis. Most previous catalytic studies of AuNPs remove the ligand shell prior to catalysis.[29–31] This is because many AuNPs synthetic methods use bulky ligands or polymers to stabilize the NPs. In addition to providing accessibility to the surface of the NP without requiring removal, it has also been proposed that the electron donating properties of the phosphine could enhance the catalytic activity of these NPs.[32] This was attributed to the increased electron density on the edges of the Au(111) faces that lowers the energy barrier required to split the O_2 double bond.

Multiple metals have been used with the Au55 synthetic method to produce monometallic NPs with 55 atoms,[33] however, there have been no examples of concurrent reduction of two metals in this way. In this work, Rh was chosen to alloy with Au because Rh55 has been made as well, and the binding energies of O_2 and the hydroxyl intermediate on Rh are predicted to be favorable.[18] According to the plot in Figure 1.3, Au and Rh lie on opposite sides of Pt for an ideal ORR catalyst, so it is reasonable to expect that an alloy of Au and Rh will have increased ORR activity compared to either monometallic catalyst independently. A similar plot can be made for an alloy of two metals. It can be seen in Figure 1.5 that at an active site containing Au_2Rh, there is higher activity for ORR compared to Au and Rh as well as other alloy compositions of Au and Rh.

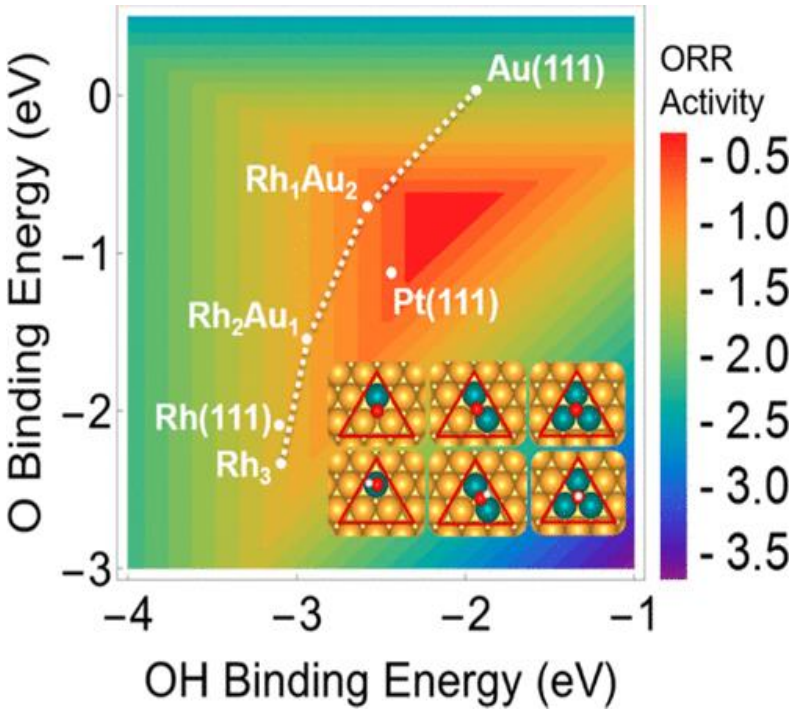

Figure 1.5: Plot of oxygen and hydroxyl binding energies compared to ORR activity. The inset shows the active sites for each composition. Gold, teal, red, and white represent Au, Rh, O, and H respectively.[20]

REFERENCES

(1)Carbon Dioxide Emissions From Energy Consumption by Source. *U.S. Energy Inf. Adm.* **2011**.

(2) Ji, Y.; Dong, H.; Liu, C.; Li, Y. The Progress of Metal-Free Catalysts for the Oxygen Reduction Reaction Based on Theoretical Simulations. *J. Mater. Chem. A* **2018**, *6* (28), 13489–13508.

(3) Gewirth, A. A.; Thorum, M. S. Electroreduction of Dioxygen for Fuel-Cell Applications: Materials and Challenges. *Inorg. Chem.* **2010**, *49* (8), 3557–3566.

(4) Gasteiger, H. A.; Markovic, N. M. Just a Dream-Or Future Reality? *Science.* **2009**, *324*, 48–49.

(5) Kraytsberg, A.; Ein-Eli, Y. Review of Advanced Materials for Proton Exchange Membrane Fuel Cells. *Energy and Fuels* **2014**, *28* (12), 7303–7330.

(6) Luo, J.; Wang, L.; Mott, D.; Njoki, P. N.; Kariuki, N.; Zhong, C. J.; He, T. Ternary Alloy Nanoparticles with Controllable Sizes and Composition and Electrocatalytic Activity. *J. Mater. Chem.* **2006**, *16* (17), 1665–1673.

(7) Shao, M.; Chang, Q.; Dodelet, J. P.; Chenitz, R. Recent Advances in Electrocatalysts for Oxygen Reduction Reaction. *Chem. Rev.* **2016**, *116* (6), 3594–3657.

(8) Geng, D.; Lu, G. Size Effect of Gold Nanoparticles on the Electrocatalytic Oxidation of Carbon Monoxide in Alkaline Solution. *J. Nanoparticle Res.* **2007**, *9* (6), 1145–1151.

(9) Lamoth, M.; Plodinec, M.; Scharfenberg, L.; Wrabetz, S.; Girgsdies, F.; Jones, T.; Rosowski, F.; Horn, R.; Schlögl, R.; Frei, E. Supported Ag Nanoparticles and Clusters for CO Oxidation: Size Effects and Influence of the Silver-Oxygen Interactions. *ACS Appl. Nano Mater.* **2019**, *2*, 2909–2920.

(10) Kim, C.; Jeon, H. S.; Eom, T.; Jee, M. S.; Kim, H.; Friend, C. M.; Min, B. K.; Hwang, Y. J. Achieving Selective and Efficient Electrocatalytic Activity for CO2 Reduction Using Immobilized Silver Nanoparticles. *J. Am. Chem. Soc.* **2015**, *137* (43), 13844–13850.

(11) Dong, C.; Lian, C.; Hu, S.; Deng, Z.; Gong, J.; Li, M.; Liu, H.; Xing, M.; Zhang, J. Size-Dependent Activity and Selectivity of Carbon Dioxide Photocatalytic Reduction over Platinum Nanoparticles. *Nat. Commun.* **2018**, *9*, 1–11.

(12) Pieta, I. S.; Rathi, A.; Pieta, P.; Nowakowski, R.; Hołdynski, M.; Pisarek, M.;

Kaminska, A.; Gawande, M. B.; Zboril, R. Electrocatalytic Methanol Oxidation over Cu, Ni and Bimetallic Cu-Ni Nanoparticles Supported on Graphitic Carbon Nitride. *Appl. Catal. B Environ.* **2019**, *244* (November 2018), 272–283.

(13) Bergamaski, K.; Pinheiro, A. L. N.; Teixeira-Neto, E.; Nart, F. C. Nanoparticle Size Effects on Methanol Electrochemical Oxidation on Carbon Supported Platinum Catalysts. *J. Phys. Chem. B* **2006**, *110*, 19271–19279.

(14) Garlyyev, B.; Kratzl, K.; Rück, M.; Michalička, J.; Fichtner, J.; Macak, J. M.; Kratky, T.; Günther, S.; Cokoja, M.; Bandarenka, A. S.; et al. Optimizing the Size of Platinum Nanoparticles for Enhanced Mass Activity in the Electrochemical Oxygen Reduction Reaction. *Angew. Chemie - Int. Ed.* **2019**, *58*, 9596–9600.

(15) Alba-Molina, D.; Puente Santiago, A. R.; Giner-Casares, J. J.; Rodríguez-Castellón, E.; Martín-Romero, M. T.; Camacho, L.; Luque, R.; Cano, M. Tailoring the ORR and HER Electrocatalytic Performances of Gold Nanoparticles through Metal-Ligand Interfaces. *J. Mater. Chem. A* **2019**, *7*, 20425–20434.

(16) Chandran, P.; Ghosh, A.; Ramaprabhu, S. High-Performance Platinum-Free Oxygen Reduction Reaction and Hydrogen Oxidation Reaction Catalyst in Polymer Electrolyte Membrane Fuel Cell. *Sci. Rep.* **2018**, *8*, 1–11.

(17) Cao, Z. qian; Wu, M. zai; Hu, H. bo; Liang, G. jin; Zhi, C. yi. Monodisperse Co9S8 Nanoparticles in Situ Embedded within N, S-Codoped Honeycomb-Structured Porous Carbon for Bifunctional Oxygen Electrocatalyst in a Rechargeable Zn–Air Battery. *NPG Asia Mater.* **2018**, *10*, 670–684.

(18) Nørskov, J. K.; Rossmeisl, J.; Logadottir, A.; Lindqvist, L.; Kitchin, J. R.; Bligaard, T.; Jónsson, H. Origin of the Overpotential for Oxygen Reduction at a Fuel-Cell Cathode. *J. Phys. Chem. B* **2004**, *108* (46), 17886–17892.

(19) Chen, W.; Chen, S. Oxygen Electroreduction Catalyzed by Gold Nanoclusters: Strong Core Size Effects. *Angew. Chemie - Int. Ed.* **2009**, *48* (24), 4386–4389.

(20) Li, H.; Luo, L.; Kunal, P.; Bonifacio, C. S.; Duan, Z.; Yang, J. C.; Humphrey, S. M.; Crooks, R. M.; Henkelman, G. Oxygen Reduction Reaction on Classically Immiscible Bimetallics: A Case Study of RhAu. *J. Phys. Chem. C* **2018**, *122* (5), 2712–2716.

(21) Kulkarni, A.; Siahrostami, S.; Patel, A.; Nørskov, J. K. Understanding Catalytic Activity Trends in the Oxygen Reduction Reaction. *Chem. Rev.* **2018**, *118* (5), 2302–2312.

(22) Schmid, G. Hexachlorododecakis(Triphenylphosphine)Pentapentacontagold, Au55(PPh3)12Cl6. *Inorg. Synth.* **1990**, *27*, 214–218.

(23) Boyen, H.; Kästle, G.; Koslowski, B.; Dietrich, C.; Ziemann, P.; Spatz, J. P.; Riethmüller, S.; Hartmann, C. Oxidation-Resistant Gold-55 Clusters. *Science.* **2002**, *297*, 1533–1536.

(24) Zhang, H.; Mautes, D.; Hartmann, U. A Study of Charge Quantization on Ligand-Stabilized Au55 Cluster Monolayers. *New J. Phys.* **2003**, *5*, 30.1-30.7.

(25) Wang, L.; Tang, Z.; Yan, W.; Yang, G.; Wang, Q.; Chen, S. Porous Carbon-Supported Gold Nanoparticles for Oxygen Reduction Reaction: Effects of Nanoparticle Size. *Appl. Mater. Interfaces* **2016**, *8*, 20635–20641.

(26) Tang, W.; Lin, H.; Kleiman-Shwarsctein, A.; Stucky, G. D.; McFarland, E. W. Size-Dependent Activity of Gold Nanoparticles for Oxygen Electroreduction in Alkaline Electrolyte. *J. Phys. Chem. C* **2008**, *112* (28), 10515–10519.

(27) Zhang, C.; Hwang, S. Y.; Peng, Z. Size-Dependent Oxygen Reduction Property of Octahedral Pt-Ni Nanoparticle Electrocatalysts. *J. Mater. Chem. A* **2014**, *2* (46), 19778–19787.

(28) Zhao, P.; Li, N.; Astruc, D. State of the Art in Gold Nanoparticle Synthesis. *Coord. Chem. Rev.* **2013**, *257* (3–4), 638–665.

(29) Lee, Y.; Loew, A.; Sun, S. Surface- and Structure-Dependent Catalytic Activity of Au Nanoparticles for Oxygen Reduction Reaction. *Chem. Mater.* **2010**, *22* (3), 755–761.

(30) Lu, L.; Lou, B.; Zou, S.; Kobayashi, H.; Liu, J.; Xiao, L.; Fan, J. Robust Removal of Ligands from Noble Metal Nanoparticles by Electrochemical Strategies. *ACS Catal.* **2018**, *8* (9), 8484–8492.

(31) Wu, L.; Xi, Z.; Sun, S. *Well-Defined Metal Nanoparticles for Electrocatalysis*, 1st ed.; Elsevier B.V., 2017.

(32) Pei, Y.; Shao, N.; Gao, Y.; Zeng, X. C. Investigating Active Site of Gold Nanoparticle Au55(PPh3)12Cl6 in Selective Oxidation. *ACS Nano* **2010**, *4* (4), 2009–2020.

(33) Schmid, G.; Klein, N.; Korste, L.; Kreibig, U.; Schönauer, D. Large Transition Metal Clusters-VI. Ligand Exchange Reactions on Au55(PPh3)12Cl6-the Formation of a Water Soluble Au55 Cluster. *Zeitschrift fur Naturforsch.* **1986**,

41b, 1028–1032.

Chapter 2: Synthesis and Electrocatalysis of Au-Rh NPs

2.1 Introduction

The properties of metallic NPs can be greatly altered with the addition of another metal into the NP. In the bulk, there are many different combinations of metals that can form alloys. These bulk alloys can have a wide range of compositions and crystal structures. Compared to bulk metals, the electronic properties of NPs change as their size decreases; quantum confinement effects become prominent for NPs <10 nm in diameter. This is because the diffuse valence bands caused by mobile electrons in bulk metals get closer to distinct energy levels as NPs get smaller.[1] NP alloys also demonstrate these size-dependent characteristics, but they are more intriguing due to the difference in structure and electronic properties of the NPs compared to their monometallic counterparts.[2]

Alloys of Au and Rh have been studied less extensively compared to other alloys of noble metals. This is largely due to the immiscibility of Au and Rh in the bulk. The bulk phase diagrams of Au and Rh indicate that the two metals will not alloy unless the synthesis is performed at temperatures well over 1000 °C.[3] Furthermore, there are few examples of Au-Rh alloyed NPs. One study reports an aqueous synthesis of Au-Rh NPs using the chloride salts and sodium borohydride to produce NPs with a range of compositions based on the molar ratios of Au and Rh.[4] Another study synthesized Au-Rh NPs with the aid of bulky dendrimers to stabilize the NPs after reduction of the metal salts.[5] Previous work within our group has synthesized similar Au-Rh alloys using a microwave assisted method and capped with polyvinylpyrrolidone.[6–8] The method used for the synthesis of Au-Rh alloys in the work discussed here, which has been previously used to make Au55[9] and Rh55,[10] involves the co-reduction of metal phosphine precursors with diborane.

The interest in the AuRh alloy system stems from the fact that Rh has been shown to be an active metal for numerous types of catalysis, including hydrogenation,[11] dehydrogenation,[12] hydroformylation,[13] and H_2 evolution.[14] Alloys of Au and Rh have mainly been used to increase catalytic activity for reactions where pure Rh has been employed. For example, it was found that Au-Rh alloys were better cyclohexene hydrogenation catalysts compared to monometallic Rh NPs.[8] The binding energies of O_2 on monometallic Au and Rh are too weak and too strong respectively for them to be attractive ORR catalysts; the overpotential required for ORR to proceed on Au and Rh is still hundreds of millivolts higher than Pt based catalysts. By tuning the binding energies of active sites with low O_2 affinity by incorporating metals with high O_2 binding, affording the design and synthesis of efficient catalysts.

2.2 Synthesis of Phosphine-Capped Au-Rh Alloys

Au55 and Rh55 were synthesized according to a previously published procedure.[9] Briefly, diborane is generated and slowly introduced into a solution of the metal-phosphine complex. The slow addition of diborane allows the reduced metal atoms to form NPs with 55 atoms, which corresponds to a two-shell cuboctahedron. The advantage of this synthetic method compared to others is the increased control of the NPs size and monodispersity. It is important to note that these are not molecular clusters–cluster with a defined molecular formula, such as $Au_{11}(PPh_3)_7Cl_3$–[15] and there is still a small distribution of sizes from the synthesis. From TEM images (Figure 2.1), the average size of Au55 synthesized is 1.5 ± 0.2 nm and the average size of Rh55 synthesized is 1.4 ± 0.2 nm. These are in agreement with the literature value for the diameter of the metal core in Au55 and Rh55, 1.4 nm and 1.3 nm respectively; and the literature value for the diameter of Au55 including the phosphine ligands is 2.1 nm.[16]

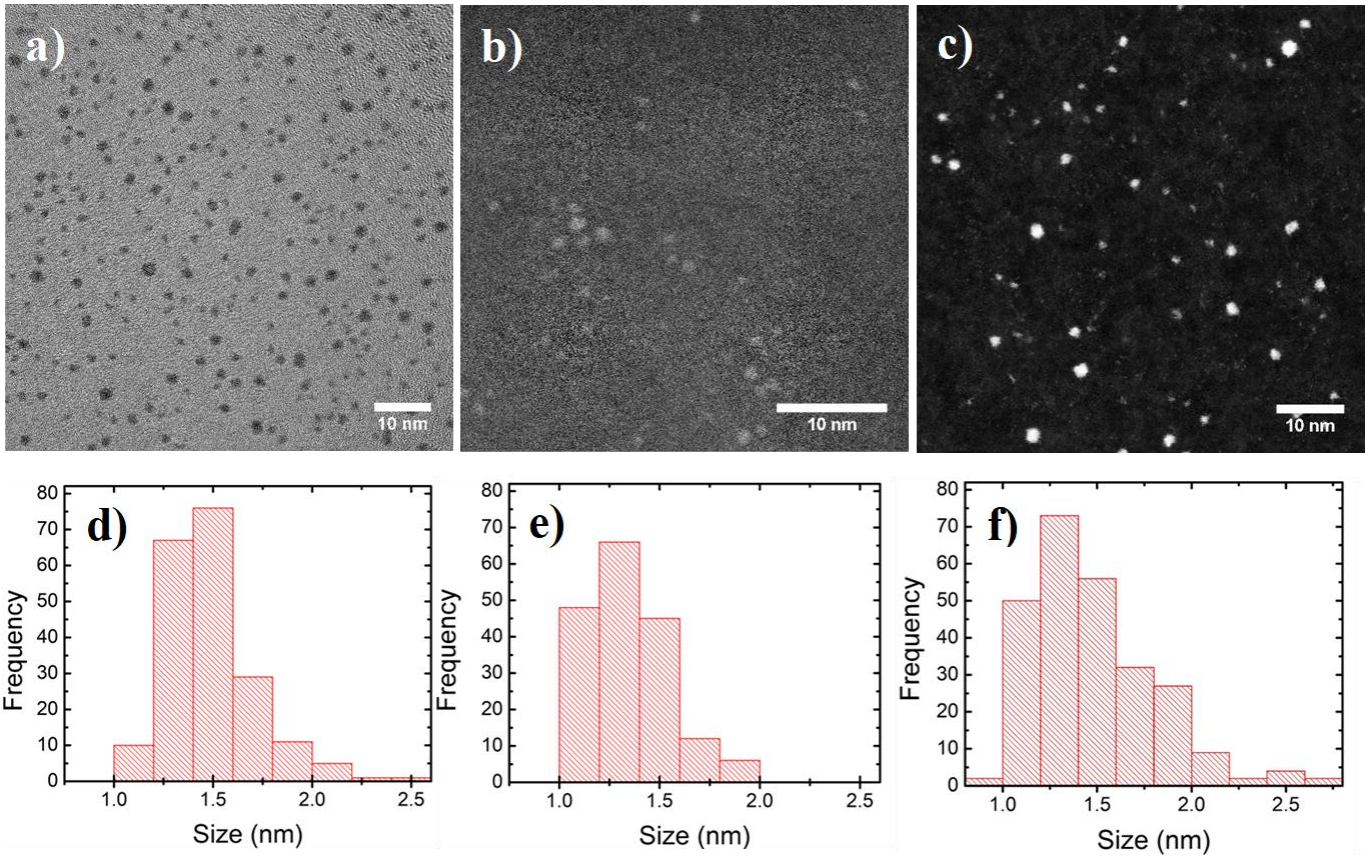

Figure 2.1: TEM/STEM images of a) Au55, b) Rh55, and c) Au-Rh NPs corresponding size distributions for d) Au55, e) Rh55, and f) Au-Rh NPs.

The Au-Rh NPs were synthesized using the same general method as Au55 and Rh55.[9,10] Two ratios of Au:Rh were used to synthesize the alloys; the molar ratios of metal precursors used were 1:1 and 2:1 Au:Rh. There have been multiple Au-Rh alloys synthesized as mentioned above, but the Au and Rh phosphine precursors have not been co-reduced by this method. Rh was chosen to alloy with Au, even though Au and Rh are immiscible in the bulk, because both $Au_{55}(PPh_3)_{12}Cl_6$ and $Rh_{55}(PPh_3)_{12}Cl_6$ have been synthesized previously. The size of both the AuRh and Au_2Rh alloys synthesized was 1.5 ± 0.3 nm from STEM images (Figure 2.2). The AuRh and Au_2Rh samples were sized

together based on the similarities between the two samples that will be discussed below. Compared to the Au55 and Rh55 size distributions, the size distributions for the alloys exhibit a larger tail due to the presence of some larger NPs (~2-2.5 nm). There were also smaller clusters ~1 nm in diameter which were identified by EDS to be Rh-rich alloys or monometallic Rh clusters. The presence of these clusters is consistent with one example of a Au-Rh alloy that was determined to have Rh clusters based on EXAFS data which showed an abnormally low Rh-Rh coordination number.[17]

The NP alloy compositions were determined by EDS (Table 2.1). The alloys synthesized were very heterogeneous; the standard deviation of the 1:1 and 2:1 Au:Rh samples was 31% and 35%, respectively. This composition was determined by point ID scans from 30 randomly selected NPs to determine the composition of individual particles that were then averaged. It is important to note that EDS of individual NPs showed a wide range of compositions that included monometallic Au and Rh NPs as well as alloys of all compositions ranging from Au-rich to Rh-rich alloys. In the EDS overlay of STEM micrographs shown in Figure 2.2**,** there are monometallic Au and Rh particles as well as some alloys visible. During the data collection, there was significant sample drift, which resulted in the element maps not being perfectly overlapped with the corresponding STEM image.

Au:Rh	Average composition (%)	STD (%)
1:1	$Au_{41}Rh_{59}$	31
2:1	$Au_{74}Rh_{26}$	35

Table 2.1: Average compositions of Au-Rh alloys determined by EDS.

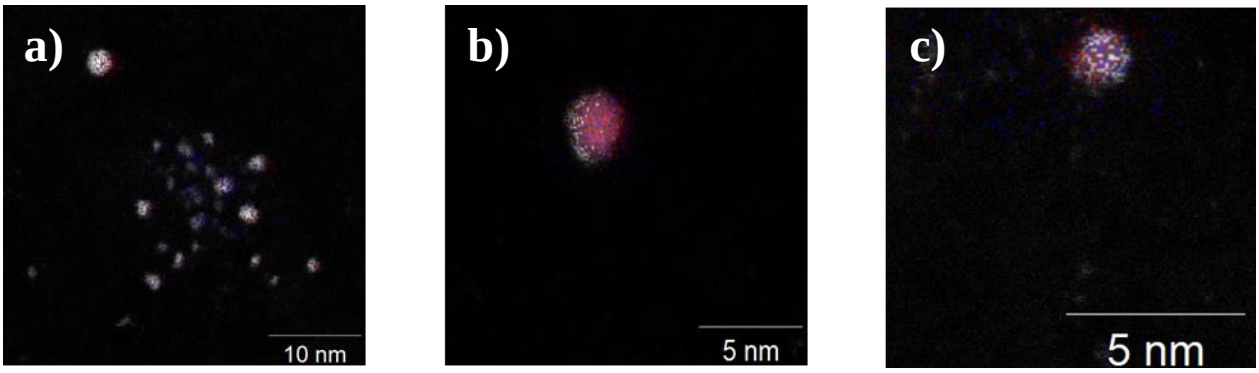

Figure 2.2: EDS overlays of a) & b) NPs synthesized from 1:1 Au:Rh precursors and c) NPs synthesized from 2:1 Au:Rh precursors. Red and blue represent Au and Rh respectively.

The EDS data showed no preference for composition and structure of the NPs, and indicate that this synthesis results in a random alloy as opposed to a core-shell or segregated Au-Rh structure. Based on the EDS analysis, the alloyed particles have a random distribution of Au and Rh atoms; there is no prevalent structure observed throughout the sample besides the random alloy. Even though both Au and Rh appear in the EDS, the resolution is an issue due to the size of these NPs. Therefore, it is not possible to conclude if there is a predominant alloy structure based on this data alone.

We hypothesized that Rh may have a preference to be in the outer shell of the NPs, as Rh is known to coordinate to phosphines more strongly than Au. Due to the relatively weak coordination of Au-P, the phosphines can dissociate from Au55 in solution, leading to the instability of Au55 in solution overtime. If Rh was at the corners of the Au-Rh NPs, the stronger coordination to the ligand shell would allow the particles to be more stable in solution over longer periods of time.

These results are consistent with a study performed by Duan *et al*. that performed multiple structural characterizations of Au-Rh alloys of ~3-5 nm in diameter and observed

a bimodal distribution of NPs in the sample.[17] Specifically, the sample consisted of both Rh NPs <1 nm and 3-5 nm Au-Rh alloys. In this study, the STEM and EDS analyses of these NPs also suggested pure RhNPs, pure AuNPs and Au-Rh alloys. The results observed in this study are similar to a theoretical study by Wang *et al*. in which the most favorable structure for the Au-Rh system for cuboctohedral and icosahedral NP morphologies were analyzed.[18] The calculations were done on NPs with over 5000 atoms corresponding to ~6 nm in diameter. In those large particles, it was determined that there was a large segregation between Au and Rh, which was due to a difference in surface energy between the metals. Also, there was a preference for Au to be further towards the core compared to the outer layers. Comparing that system to the one synthesized in this work is more challenging because that theoretical system has approximately 100 times more atoms than the system discussed in this work. Furthermore, there has not been any segregation of elements observed in the alloyed particles in this work; ther is no indication of one metal having a preference to be in the core or the shell of the NPs. It is noteworthy that the NPs in this work would theoretically have 55 atoms, 42 of which would be surface atoms. Even if each AuRh NP had an ideal composition of $Au_{27}Rh_{28}$ and the core was all Au, there would still be 14 Au atoms on the surface. This may be a reason that there are random alloys observed rather than an ordered alloy structure given that EDS is a surface technique.

^{31}P-NMR was performed on the samples and the results are shown in Figure 2.3. Au55 showed a single peak at 32.68 ppm, while Rh55 showed a broad peak around 19 ppm. Both the 1:1 and 2:1 samples of Au:Rh showed only a single peak at 32.68 ppm. This would suggest that there is a significant amount of Au on the surface to coordinate to the phosphines. However, it was expected that both Au-P and Rh-P peaks would be present based on the EDS data that indicated the presence of pure Au and Rh NPs as well as the alloys. It could be possible that there is not a high enough concentration of the pure Rh NPs

to overcome the background of the NMR signal; however, if these alloys were all random alloys, there would be no preference for Au or Rh to be on the surface and it would be reasonable to predict that some Rh would be on the surface of the NPs and therefore coordinated to the phosphines. However, because there is no Rh-P peak present in the NMR, the data alone suggests that there may be a preference for Au to be at the surface of these particles. This finding is in contrast to the EDS data discussed earlier. This could be due to the limited resolution of EDS due to the size of these NPs. There was background present in Figure 2.2 which prevents an accurate determination of the structure from that data.

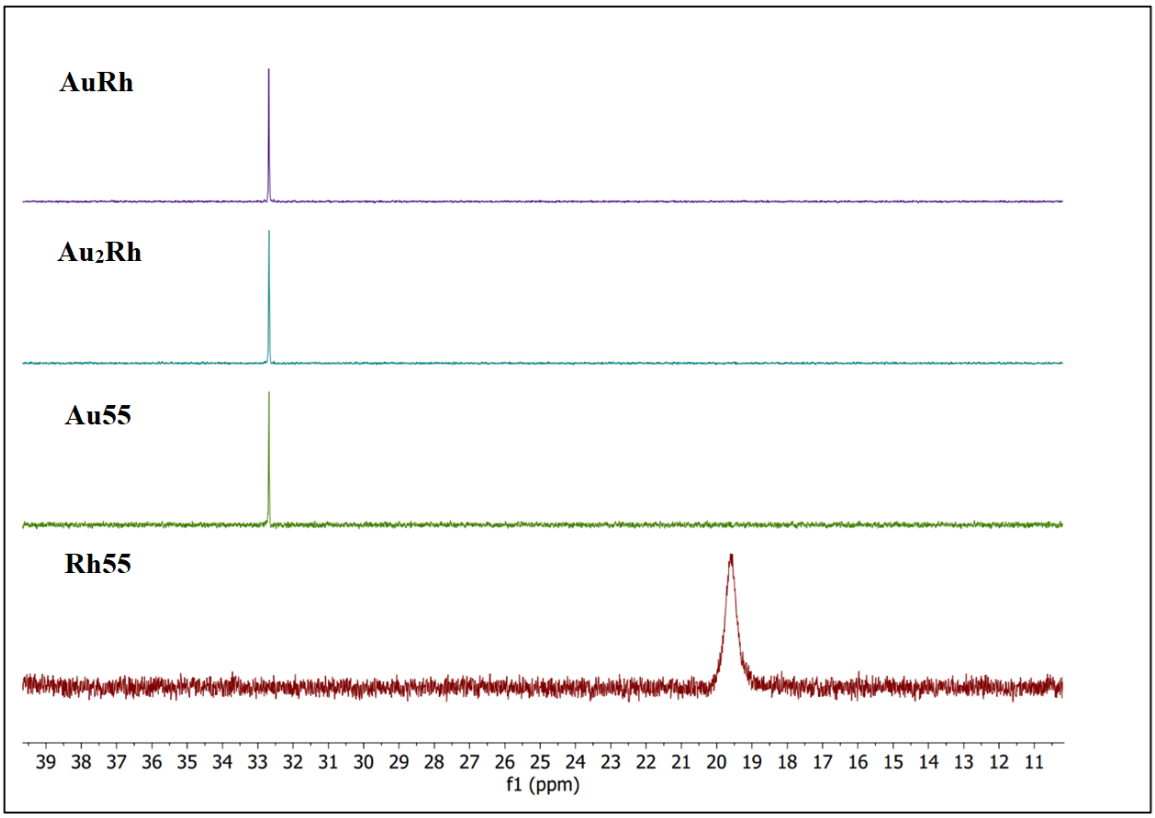

Figure 2.3: Stacked NMR spectra of Rh55, Au55, Au_2Rh, and AuRh NPs synthesized. NMR spectra were collected at -50°C.

The Au-Rh alloys were also characterized by TOF-SIMS, which is a variant of mass spectrometry that can be utilized to examine the surface composition of a sample with high resolution by sequentially sputtering a layer of atoms at a time off of the surface of the sample. The NPs were dropcast onto a silicon wafer and allowed to dry in air. Comparing the NMR and TOF-SIMS data was able to provide a better overall picture for the structure of the NPs. It can be seen in Figure 2.4 that in both compositions of alloys, there is a large spike in Au intensity within the first few seconds of sputtering time, followed by a gradual increase over time of the Rh intensity before the intensity of both elements achieve a constant value. This initial spike in Au intensity indicates that there is a larger amount of Au on the surface of the alloys that is sputtered off before reaching any Rh in the samples. The intensities plotted were normalized to the maximum of each element. Furthermore, the intensities are not directly related to Au/Rh composition of the alloys as a whole because the plot only shows at what time each element is at its maximum. TOF-SIMS is a very surface sensitive technique, and because these NPs are smaller than 5 nm, the first few seconds of sputtering is the most useful in determining composition of the sample's

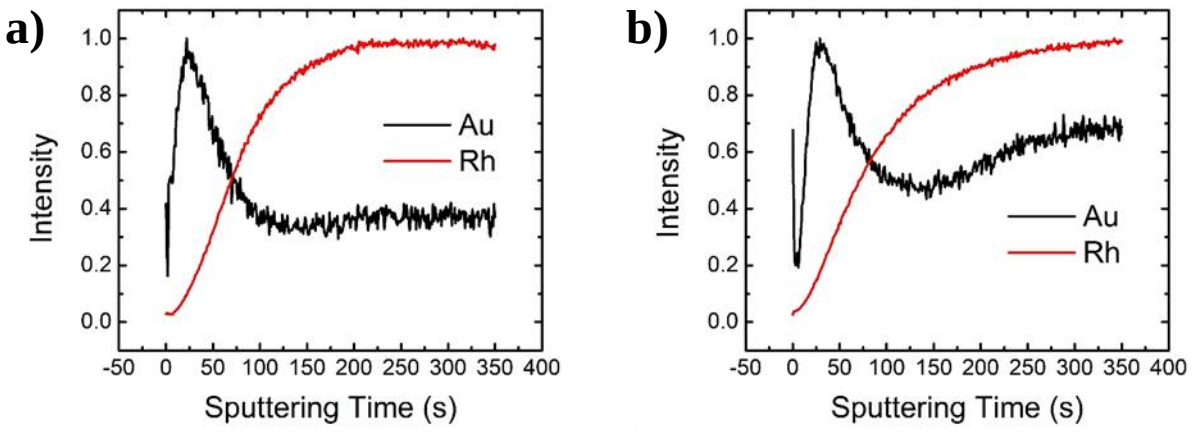

Figure 2.4: Intensity vs. sputtering time for a) 1:1 and b) 2:1 Au:Rh compositions from TOF-SIMS.

surface. This is because dropcasting does not create a uniform film of the sample, so there are multiple layers of NPs stacked on one another. Consequently, as we sputter deeper into the sample, the TOF-SIMS data becomes more indicative of bulk composition rather than surface composition, which is why each metal intensity starts to level off as the sputtering time increases.

The TOF-SIMS data is in agreement with the NMR data that also indicated that there was significant amounts of Au on the surface due to the absence of any Rh-P peaks in the NMR. It is possible that the inconsitency seen in the EDS data compared to NMR and TOF-SIMS is due to NP instability under the electron beam in STEM. During EDS analysis, it is possible that there is some rearrangement of the atoms in the NPs that could lead to random alloys or potentially de-alloying of the NPs.

2.3 ELECTROCATALYSIS OF AU-RH ALLOYS

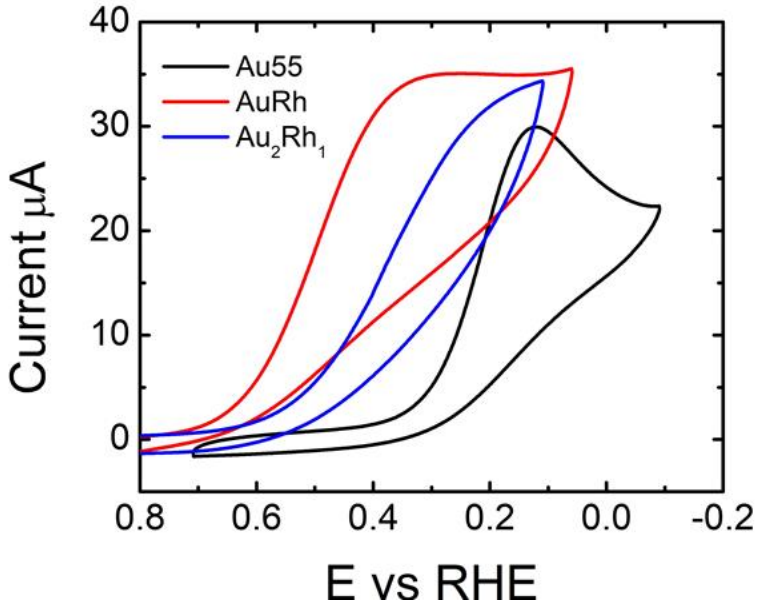

Figure 2.5: CVs of Au-Rh alloys and Au55 in O_2-saturated 0.1 M $HClO_4$ at 50 mV/s scan rate.

The electrocatalytic activity towards ORR was measured for the alloys discussed in the previous section and compared with the activities of Au55 and Rh55. The activity was first measured by cyclic voltammetry (CV), and then kinetic studies using RRDV were performed. For CV measurements, the electrodes were prepared dispersing the NPs so each had the same NP concentration of 70 μM and 10 μL was drop-cast onto the working electrode. The working electrode was a glassy carbon disk, and the counter electrode was a glassy carbon rod. All potentials reported have been converted to be reference to the reversible hydrogen electrode (RHE). The CVs in Figure 2.5 show a positive shift in the onset potential for ORR–towards the standard reduction potential of +1.23 V–for the alloys compared to Au55.

RRDV was also used to study these alloys. This method provides information similar to the CVs along with an additional current from a Pt ring that is set at a potential sufficient to oxidize any H_2O_2 generated by the catalyst on the working electrode. Consequently, the current generated at the Pt ring correlates to the amount of H_2O_2 produced by the catalysts. As mentioned above, if the number of electrons is closer to 2 or 4, more H_2O_2 or O_2 is being produced, respectively. The number of electrons involved in the ORR pathway of each catalyst was calculated using the equation in reference 18, which is derived from the Levich equation.[19]

Based on previous literature studies,[7,20] one would predict that this activity increase is due to the alloying of Au and Rh based on the effects that alloying has on the surface energy of NPs. It has been calculated that the Au_2Rh_1 site is expected to have the highest activity for ORR.[7] That theoretical result is not what was observed in this system. The AuRh alloy has higher ORR activity compared to Au_2Rh. The EDS indicated that the alloy compositions between samples was completely random. If this were the case that the particles contributing to the ORR activity were of random composition, one would expect

both alloy samples to have the same activity. The NMR and TOF-SIMS data indicated that both alloy samples similarly had more Au on the surface than Rh; from that data, it is reasonable to say that both samples are similar so there should be similar ORR activity.

We hypothesized that the alloys would show a greater activity than either monometallic NP; we also hypothesized that the alloys would perform the ORR *via* a number of electrons transferred closer to four, whereas Au55 and Rh55 would favor the two electron transfer pathway. The ORR polarization curves for all four samples are shown in Figure 2.6; overpotentials and electrons transferred are listed in Table 2.2. Surprisingly,

Rh55 had the lowest overpotential required for the ORR, the most electrons transferred, and the highest limiting current. Based on the plot in Figure 1.3 and past studies,[7,21] Rh55 would be expected to have ORR activity that is comparable to Au55. The

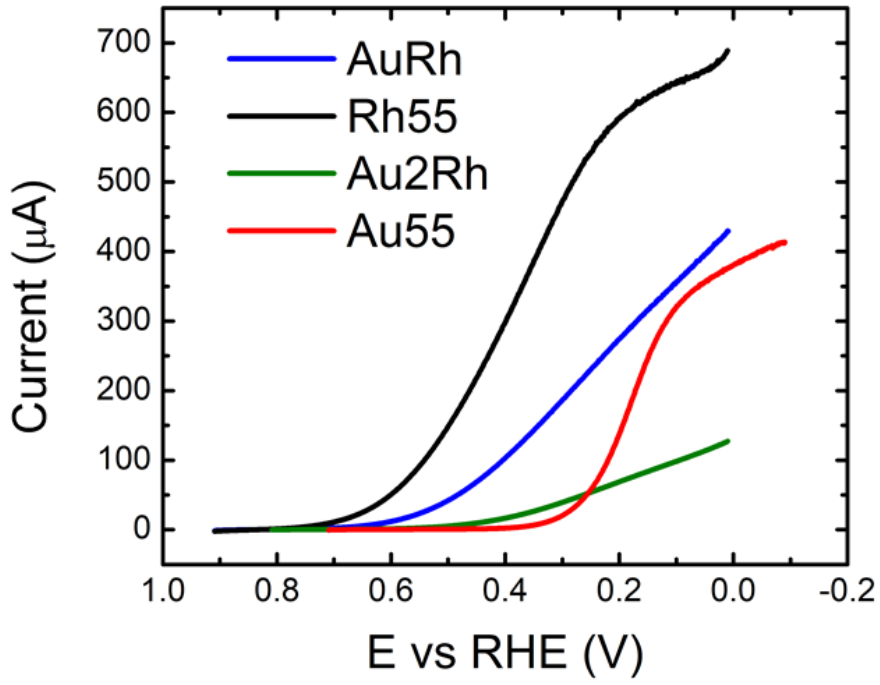

Figure 2.6: ORR polarization curves of each catalyst in O_2-saturated 0.1 M $HClO_4$ at 5 mV/s scan rate.

Sample	η (mV)	n
Au55	945 ± 2	2.31 ± 0.11
Au_2Rh	890 ± 2	2.74 ± 0.08
AuRh	672 ± 5	3.13 ± 0.05
Rh55	590 ± 3	3.71 ± 0.06

Table 2.2: Overpotentials (η) and number of electrons (n) for each catalyst that was synthesized. Overpotential was measured where the current reached 30 μA for each catalyst.

other three samples followed the trend that was seen in the CVs with AuRh having the best ORR activity. Also, as the overpotential decreased, the number of electrons transferred for each catalyst increased.

It is possible that the alloys synthesized do not significantly contribute to the ORR activity–it is possible that the trend seen in these four samples is primarily based on the percentage of Rh in the sample, where increasing amounts of Au dilute the catalytic activity of the pure Rh rather than enhancing the active sites of the alloy catalyst. From the EDS shown above in Figure 2.2, there are monometallic Rh particles present in both alloyed samples, which could be the active catalyst in the samples. Catalysis happens at the surface of NPs, so if there is more surface Au in the Au_2Rh sample compared to the AuRh sample, the AuRh sample would be expected to have a higher activity. If the active catalyst is pure Rh, the limiting currents of the alloyed samples and Rh55 can be attributed to the Rh content in each sample. The AuRh sample might have a higher limiting current compared to Au_2Rh simply due to the higher Rh % and a larger amount of pure RhNPs.

To test the stability of the Au-Rh NPs, STEM images were taken of the catalyst after multiple ORR cycles. It can be seen from Figure 2.7 that the majority of the NPs

retained their diameter of ~1.4 nm. However, there are larger NPs that appeared after ORR that were not observed in STEM images of the Au-Rh NPs prior to catalysis. After multiple cycles of ORR during the RRDV experiments, there was minimal deviation in onset or peak potentials, suggesting that the catalysts are stable during ORR; however, the appearance of larger particles in the STEM images post-catalysis indicates that there is decreased stability of the catalysts after multiple cycles. In a recent study examining the stability of AuNPs after CO_2 reduction,[22] it was found that citrate-capped AuNPs (~2 nm) exhibited significant growth after electrocatalysis, consistent with the results shown above.

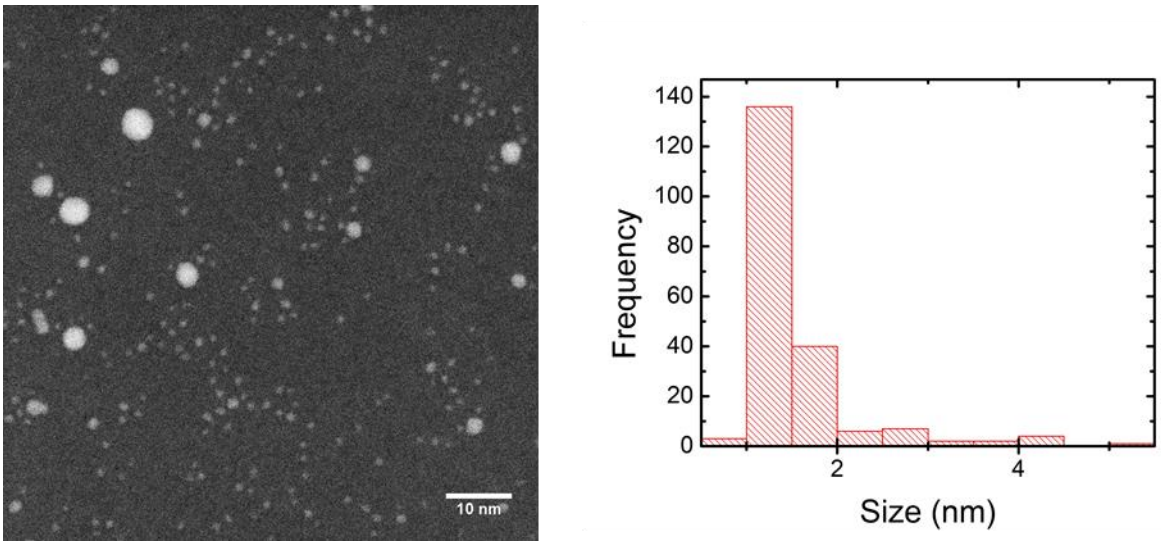

Figure 2.7: STEM image and size distribution of AuRh sample after ORR cycling.

2.4 CONCLUSION

In this work, two new Au-Rh alloys were synthesized from different ratios of metal precursors using the same method to synthesize Au55 and Rh55 using BH_3 as a clean reductant. EDS data showed that the alloyed NPs were very heterogeneous with regards to

composition, as both samples included pure Au and Rh NPs, as well as a wide range of alloys that appeared to have a random structure. NMR and TOF-SIMS analysis indicated that there was a disproportionately high amount of Au on the surface of the NPs, accounting for the absence of any Rh-P signal in the NMR spectra and a higher Au intensity at lower sputtering times in TOF-SIMS. The electrocatalysis data showed that Rh55 was the most active catalyst for ORR and that the AuRh sample had a higher activity than the Au_2Rh sample. This result was not expected based on results for similar alloyed systems in the literature. It looks possible that Rh NPs are the active catalyst for ORR in each sample (aside from Au55); it is not clear what effect, if any, the alloys have on ORR activity. Future work on this project includes optimization of the synthesis to attempt to homogenize the distribution of NP composition to produce only alloyed NPs. Additionally, different phosphines could be exchanged for triphenylphosphine to examine the effects of electron donating or withdrawing properties on the core of the NP in order to fine-tune the catalytic activity.

2.5 EXPERIMENTAL

2.5.1 Materials and Methods

$HAuCl_4 \cdot 3H_2O$ (99%, Strem) and $RhCl_3 \cdot 3H_2O$ (99%, Strem) were used as received. PPh_3 (99%, Sigma Aldrich) was recrystallized from hot EtOH and vacuum dried in a desiccator overnight before using. Dichloromethane (DCM) was distilled over CaH_2 in a nitrogen atmosphere and stored over 4A molecular sieves. Dimethoxyethane (DME) was distilled over $CaCl_2$ in a nitrogen atmosphere and stored over 4A molecular sieves. Pentane and benzene were degassed and stored over 4A molecular sieves before use. All synthesis was performed under a nitrogen atmosphere.

2.5.2 Synthesis of $AuCl(PPh_3)$

$AuCl(PPh_3)$ was synthesized according to a previously published procedure.[23] 1.010 g $HAuCl_4 \cdot 3H_2O$ (2.54 mmol) was dissolved in 35 mL 95% degassed EtOH. In a separate flask, 1.364 g PPh_3 (5.20 mmol) was dissolved in 50 mL 95% degassed EtOH. The PPh_3 was added to the $HAuCl_4$ solution using a cannula. The resulting precipitate was vacuum filtered in air using a Büchner funnel, washed with Et_2O and dried in a desiccator. The white solid was then dissolved in 10 mL DCM and slowly precipitated with the addition of 60 mL pentane. The precipitate was cooled at -10°C for 30 minutes and then vacuum filtered. Yield: 0.9948 g (80%).

2.5.3 Synthesis of $RhCl(PPh_3)_3$

$RhCl(PPh_3)_3$ was synthesized according to a previously published procedure.[24] 2.000 g $RhCl_3 \cdot 3H_2O$ (7.5 mmol) was dissolved in 70 mL 95% degassed EtOH. 12.000 g PPh_3 (45.7 mmol) was dissolved in 350 mL 95% degassed hot EtOH. The PPh_3 was added using a cannula to the $RhCl_3$ solution and the solution was refluxed for 3 h. The product was vacuum filtered in air using a Büchner funnel and washed with Et_2O. Yield: 6.134 g (85%).

2.5.4 Synthesis of $Au_{55}(PPh_3)_{12}Cl_6$

$Au_{55}(PPh_3)_{12}Cl_6$ was synthesized according to a previously published procedure.[9] B_2H_6 was generated by the addition of 50 mL BF_3-$O(C_2H_5)_2$ over 45 minutes to 10 g $NaBH_4$ in 50 mL DME. The B_2H_6 was bubbled through a solution of 2.000 g $AuCl(PPh_3)$ (4 mmol) in 75 mL benzene which is heated at 60°C. After the B_2H_6 addition is complete, the solution was allowed to cool to room temperature, and then the B_2H_6 was purged from the solution and atmosphere. The solution is filtered and the solid is dissolved through the frit with 50

mL DCM. Then, that solution was filtered through a Celite column and then precipitated with the addition of 125 mL pentane over 1 h. Yield: 237 mg (23%).

2.5.5 Synthesis of $Rh_{55}(PPh_3)_{12}Cl_6$

$Rh_{55}(PPh_3)_{12}Cl_6$ was synthesized according to a previously published procedure.[10] B_2H_6 was generated with the addition of 75 mL BF_3-$O(C_2H_5)_2$ over 45 minutes to 15 g $NaBH_4$ in 75 mL DME. The B_2H_6 was bubbled through a solution of 1.0186 g $RhCl(PPh_3)_3$ (1.1 mmol) in 75 mL tetrahydrofuran which was heated at 60°C. After the B_2H_6 addition is complete, the solution was allowed to cool to room temperature, and then the B_2H_6 was purged from the solution and atmosphere. The tetrahydrofuran was then removed under vacuum and 75 mL pentane added dropwise with vigorous stirring over several hours. The product was then filtered and washed with a 2:1 pentane:benzene mixture. Yield: 122 mg (70%)

2.5.6 Synthesis of Au-Rh Alloys

The Au-Rh alloys were synthesized using the same method as $Au_{55}(PPh_3)_{12}Cl_6$. The 1:1 and 2:1 is a molar ratio of Au:Rh. For the 1:1, 0.7000 g $AuCl(PPh_3)$ (1.41 mmol) and 1.3089 g $RhCl(PPh_3)_3$ (1.41 mmol) were dissolved in 75 mL benzene at 60°C. B_2H_6 was generated with the addition of 75 mL BF_3-$O(C_2H_5)_2$ over 45 minutes to 15 g $NaBH_4$ in 75 mL DME. After the B_2H_6 addition is complete, the solution was allowed to cool to room temperature, and then the B_2H_6 was purged from the solution and atmosphere. The solution was filtered and the solid was dissolved through the filter with 50 mL DCM. Then, that solution was filtered through a Celite column and then precipitated with the addition of 125 mL pentane over 1 h. Yield: 250 mg

For the 2:1, 0.7600 g $AuCl(PPh_3)$ (1.53 mmol) and 0.7110 g $RhCl(PPh_3)_3$ (0.765 mmol) were used. B_2H_6 was generated by the addition of 50 mL BF_3-$O(C_2H_5)_2$ over 45 minutes to 10 g $NaBH_4$ in 50 mL dimethoxyethane. After the B_2H_6 addition is complete, the solution was allowed to cool to room temperature, and then the B_2H_6 was purged from the solution and atmosphere. The solution was filtered and the solid was dissolved through the filter with 50 mL DCM. Then, that solution was filtered through a Celite column and then precipitated with the addition of 125 mL pentane over 1 h. Yield: 146 mg

2.5.7 Characterization

TEM/STEM was performed with a JEOL 2010F transmission electron microscope. EDS was performed with a JEOL NEOARM Low kV STEM corrected microscope. TEM grids from Electron Microscopy Sciences (CF400-Cu-UL) were prepared by dispersing the NPs in DCM then dropcasting 2 μL on the grid and air dried. NMR was performed with an Agilent VNMRS 600 MHz instrument. The TOF-SIMS analysis is done with a Bi_3^+ beam at 30 kV, 3 pA sample current, raster scanning 100 μm x 100 μm areas. The sputtering is done with a Cs^+ ion beam at 500 V, ~40 nA sample current, raster scanning 300 μm x 300 μm areas centered over the Bi_3^+ analysis areas. The samples were dispersed in DCM and dropcast onto silicon wafers.

2.5.8 Electrocatalysis

All electrocatalysis was done with a CH Instruments CH 700E bipotentiostat. RRDV was done using a Pine Instrument Company analytical rotator (model AFASR) and Pine Instrument Company ASR speed control. The electrolyte is 0.1 M $HClO_4$, the counter electrode is a glassy carbon rod, and the reference electrode was $Hg/HgSO_4$ (MSE). All potentials shown were converted to RHE. For CV experiments, each catalyst was dispersed

with DCM to make a 70 μM dispersion. 10 μL was dropcast onto 3 mm glassy carbon electrodes and dried in air. The electrolyte (10 mL) was purged with O_2 for 30 minutes.

For RRDV, each catalyst was dispersed with DCM to make a 70 μM dispersion. 15 μL was dropcast on a 5 mm glassy carbon disk and dried in air. The electrolyte (30 mL) was purged with O_2 for 1.5 h and was constantly purging the headspace during catalysis. The potentials for Rh55 and Au-Rh NPs were scanned from 0.2 V to -0.7 V vs MSE at 5 mV/s. For Au55, the potential was scanned from 0 V to -0.8 V vs MSE. The Pt ring was held at 0.5 V vs MSE to oxidize any H_2O_2. The collection efficiency of the Pt was determine by the ratio of currents using $K_4Fe(CN)_6$.

REFERENCES

(1) Schmid, G. The Relevance of Shape and Size of Au 55 Clusters. *Chem. Soc. Rev.* **2008**, *37* (9), 1909–1930.

(2) Ferrando, R.; Jellinek, J.; Johnston, R. L. Nanoalloys: From Theory to Applications of Alloy Clusters and Nanoparticles. *Chem. Rev.* **2008**, *108* (3), 845–910.

(3) Okamoto, H.; Massalski, T. B. The Au-Rh (Gold-Rhodium) System. **1984**, *5* (4), 384–387.

(4) Essinger-Hileman, E. R.; Decicco, D.; Bondi, J. F.; Schaak, R. E. Aqueous Room-Temperature Synthesis of Au-Rh, Au-Pt, Pt-Rh, and Pd-Rh Alloy Nanoparticles: Fully Tunable Compositions within the Miscibility Gaps. *J. Mater. Chem.* **2011**, *21* (31), 11599–11604.

(5) Luo, L.; Timoshenko, J.; Lapp, A. S.; Frenkel, A. I.; Crooks, R. M. Structural Characterization of Rh and RhAu Dendrimer-Encapsulated Nanoparticles. *Langmuir* **2017**, *33* (43), 12434–12442.

(6) García, S.; Anderson, R. M.; Celio, H.; Dahal, N.; Dolocan, A.; Zhou, J.; Humphrey, S. M. Microwave Synthesis of Au–Rh Core–Shell Nanoparticles and Implications of the Shell Thickness in Hydrogenation Catalysis. *Chem. Commun.* **2013**, *49* (39), 4241–4243.

(7) Li, H.; Luo, L.; Kunal, P.; Bonifacio, C. S.; Duan, Z.; Yang, J. C.; Humphrey, S. M.; Crooks, R. M.; Henkelman, G. Oxygen Reduction Reaction on Classically Immiscible Bimetallics: A Case Study of RhAu. *J. Phys. Chem. C* **2018**, *122* (5), 2712–2716.

(8) García, S.; Zhang, L.; Piburn, G. W.; Henkelman, G.; Humphrey, S. M. Microwave Synthesis of Classically Immiscible Rhodium-Silver and Rhodium-Gold Alloy Nanoparticles: Highly Active Hydrogenation Catalysts. *ACS Nano* **2014**, *8* (11), 11512–11521.

(9) Schmid, G. Hexachlorododecakis(Triphenylphosphine)Pentapentacontagold, Au55(PPh3)12Cl6. *Inorg. Synth.* **1990**, *27*, 214–218.

(10) Schmid, G.; Klein, N.; Korste, L.; Kreibig, U.; Schönauer, D. Large Transition Metal Clusters-VI. Ligand Exchange Reactions on Au55(PPh3)12Cl6-the Formation of a Water Soluble Au55 Cluster. *Zeitschrift fur Naturforsch.* **1986**, *41b*, 1028–1032.

(11) Genna, D. T.; Pfund, L. Y.; Samblanet, D. C.; Wong-Foy, A. G.; Matzger, A. J.;

Sanford, M. S. Rhodium Hydrogenation Catalysts Supported in Metal Organic Frameworks: Influence of the Framework on Catalytic Activity and Selectivity. *ACS Catal.* **2016**, *6* (6), 3569–3574.

(12) Shih, K. C.; Goldman, A. S. Alkane Dehydrogenation Catalyzed by Rhodium(I) Phosphine Complexes: Observation of the Stoichiometric Alkane-to-Rhodium Hydrogen-Transfer Step. *Organometallics* **1993**, *12* (9), 3390–3392.

(13) Sparta, M.; Børve, K. J.; Jensen, V. R. Activity of Rhodium-Catalyzed Hydroformylation: Added Insight and Predictions from Theory. *J. Am. Chem. Soc.* **2007**, *129* (27), 8487–8499.

(14) Begum, A.; Bose, M.; Moula, G. Graphene Supported Rhodium Nanoparticles for Enhanced Electrocatalytic Hydrogen Evolution Reaction. *Sci. Rep.* **2019**, *9* (1), 1–10.

(15) Narouz, M. R.; Osten, K. M.; Unsworth, P. J.; Man, R. W. Y.; Salorinne, K.; Takano, S.; Tomihara, R.; Kaappa, S.; Malola, S.; Dinh, C. T.; et al. N-Heterocyclic Carbene-Functionalized Magic-Number Gold Nanoclusters. *Nat. Chem.* **2019**, *11* (5), 419–425.

(16) Schmid, G.; Pfeil, R.; Boese, R.; Bandermann, F.; Meyer, S.; Calis, G. H. M.; van der Velden, J. W. A. Au55[P(C6H5)3]12CI6 — Ein Goldcluster Ungewöhnlicher Größe. *Chem. Ber.* **1981**, *114*, 3634–3642.

(17) Duan, Z.; Timoshenko, J.; Kunal, P.; House, S. D.; Wan, H.; Jarvis, K.; Bonifacio, C.; Yang, J. C.; Crooks, R. M.; Frenkel, A. I.; et al. Structural Characterization of Heterogeneous RhAu Nanoparticles from a Microwave-Assisted Synthesis. *Nanoscale* **2018**, *10* (47), 22520–22532.

(18) Wang, G.; Xu, Y.; Qian, P.; Su, Y. ADP Potential for the Au-Rh System and Its Application in Element Segregation of Nanoparticles. *Comput. Mater. Sci.* **2021**, *186* (July 2020), 110002.

(19) Galyamova, A.; Shin, K.; Henkelman, G.; Crooks, R. M. Effect of TiOx Substrate Interactions on the Electrocatalytic Oxygen Reduction Reaction at Au Nanoparticles. *J. Phys. Chem. C* **2020**, *124* (18), 10045–10056.

(20) Luo, J.; Wang, L.; Mott, D.; Njoki, P. N.; Kariuki, N.; Zhong, C. J.; He, T. Ternary Alloy Nanoparticles with Controllable Sizes and Composition and Electrocatalytic Activity. *J. Mater. Chem.* **2006**, *16* (17), 1665–1673.

(21) Nørskov, J. K.; Rossmeisl, J.; Logadottir, A.; Lindqvist, L.; Kitchin, J. R.; Bligaard,

T.; Jónsson, H. Origin of the Overpotential for Oxygen Reduction at a Fuel-Cell Cathode. *J. Phys. Chem. B* **2004**, *108* (46), 17886–17892.

(22) Trindell, J. A.; Clausmeyer, J.; Crooks, R. M. Size Stability and H2/CO Selectivity for Au Nanoparticles during Electrocatalytic CO2 Reduction. *J. Am. Chem. Soc.* **2017**, *139* (45), 16161–16167.

(23) Braunstein, P.; Lehner, H.; Matt, D. A Platinum-Gold Cluster: Chloro-1κCl-Bis(Triethylphosphine-1κP)Bis(Triphenyl- Phosphine)-2κP, 3κP-Triangulo-Digold-Platinum(1 +) Trifluoromethanesulfonate. *Inorg. Synth.* **1990**, *27*, 218–221.

(24) Osborn, J. A.; Wilkinson, G. Tris(Triphenylphosphine)Halorhodium(I). *Inorg. Synth.* **1967**, *X*, 67–71.

Bibliography

CHAPTER 1

(1)Carbon Dioxide Emissions From Energy Consumption by Source. *U.S. Energy Inf. Adm.* **2011**.

(2) Ji, Y.; Dong, H.; Liu, C.; Li, Y. The Progress of Metal-Free Catalysts for the Oxygen Reduction Reaction Based on Theoretical Simulations. *J. Mater. Chem. A* **2018**, *6* (28), 13489–13508.

(3) Gewirth, A. A.; Thorum, M. S. Electroreduction of Dioxygen for Fuel-Cell Applications: Materials and Challenges. *Inorg. Chem.* **2010**, *49* (8), 3557–3566.

(4) Gasteiger, H. A.; Markovic, N. M. Just a Dream-Or Future Reality? *Science.* **2009**, *324*, 48–49.

(5) Kraytsberg, A.; Ein-Eli, Y. Review of Advanced Materials for Proton Exchange Membrane Fuel Cells. *Energy and Fuels* **2014**, *28* (12), 7303–7330.

(6) Luo, J.; Wang, L.; Mott, D.; Njoki, P. N.; Kariuki, N.; Zhong, C. J.; He, T. Ternary Alloy Nanoparticles with Controllable Sizes and Composition and Electrocatalytic Activity. *J. Mater. Chem.* **2006**, *16* (17), 1665–1673.

(7) Shao, M.; Chang, Q.; Dodelet, J. P.; Chenitz, R. Recent Advances in Electrocatalysts for Oxygen Reduction Reaction. *Chem. Rev.* **2016**, *116* (6), 3594–3657.

(8) Geng, D.; Lu, G. Size Effect of Gold Nanoparticles on the Electrocatalytic Oxidation of Carbon Monoxide in Alkaline Solution. *J. Nanoparticle Res.* **2007**, *9* (6), 1145–1151.

(9) Lamoth, M.; Plodinec, M.; Scharfenberg, L.; Wrabetz, S.; Girgsdies, F.; Jones, T.; Rosowski, F.; Horn, R.; Schlögl, R.; Frei, E. Supported Ag Nanoparticles and Clusters for CO Oxidation: Size Effects and Influence of the Silver-Oxygen Interactions. *ACS Appl. Nano Mater.* **2019**, *2*, 2909–2920.

(10) Kim, C.; Jeon, H. S.; Eom, T.; Jee, M. S.; Kim, H.; Friend, C. M.; Min, B. K.; Hwang, Y. J. Achieving Selective and Efficient Electrocatalytic Activity for CO2 Reduction Using Immobilized Silver Nanoparticles. *J. Am. Chem. Soc.* **2015**, *137* (43), 13844–13850.

(11) Dong, C.; Lian, C.; Hu, S.; Deng, Z.; Gong, J.; Li, M.; Liu, H.; Xing, M.; Zhang, J. Size-Dependent Activity and Selectivity of Carbon Dioxide Photocatalytic

Reduction over Platinum Nanoparticles. *Nat. Commun.* **2018**, *9*, 1–11.

(12) Pieta, I. S.; Rathi, A.; Pieta, P.; Nowakowski, R.; Hołdynski, M.; Pisarek, M.; Kaminska, A.; Gawande, M. B.; Zboril, R. Electrocatalytic Methanol Oxidation over Cu, Ni and Bimetallic Cu-Ni Nanoparticles Supported on Graphitic Carbon Nitride. *Appl. Catal. B Environ.* **2019**, *244* (November 2018), 272–283.

(13) Bergamaski, K.; Pinheiro, A. L. N.; Teixeira-Neto, E.; Nart, F. C. Nanoparticle Size Effects on Methanol Electrochemical Oxidation on Carbon Supported Platinum Catalysts. *J. Phys. Chem. B* **2006**, *110*, 19271–19279.

(14) Garlyyev, B.; Kratzl, K.; Rück, M.; Michalička, J.; Fichtner, J.; Macak, J. M.; Kratky, T.; Günther, S.; Cokoja, M.; Bandarenka, A. S.; et al. Optimizing the Size of Platinum Nanoparticles for Enhanced Mass Activity in the Electrochemical Oxygen Reduction Reaction. *Angew. Chemie - Int. Ed.* **2019**, *58*, 9596–9600.

(15) Alba-Molina, D.; Puente Santiago, A. R.; Giner-Casares, J. J.; Rodríguez-Castellón, E.; Martín-Romero, M. T.; Camacho, L.; Luque, R.; Cano, M. Tailoring the ORR and HER Electrocatalytic Performances of Gold Nanoparticles through Metal-Ligand Interfaces. *J. Mater. Chem. A* **2019**, *7*, 20425–20434.

(16) Chandran, P.; Ghosh, A.; Ramaprabhu, S. High-Performance Platinum-Free Oxygen Reduction Reaction and Hydrogen Oxidation Reaction Catalyst in Polymer Electrolyte Membrane Fuel Cell. *Sci. Rep.* **2018**, *8*, 1–11.

(17) Cao, Z. qian; Wu, M. zai; Hu, H. bo; Liang, G. jin; Zhi, C. yi. Monodisperse Co9S8 Nanoparticles in Situ Embedded within N, S-Codoped Honeycomb-Structured Porous Carbon for Bifunctional Oxygen Electrocatalyst in a Rechargeable Zn–Air Battery. *NPG Asia Mater.* **2018**, *10*, 670–684.

(18) Nørskov, J. K.; Rossmeisl, J.; Logadottir, A.; Lindqvist, L.; Kitchin, J. R.; Bligaard, T.; Jónsson, H. Origin of the Overpotential for Oxygen Reduction at a Fuel-Cell Cathode. *J. Phys. Chem. B* **2004**, *108* (46), 17886–17892.

(19) Chen, W.; Chen, S. Oxygen Electroreduction Catalyzed by Gold Nanoclusters: Strong Core Size Effects. *Angew. Chemie - Int. Ed.* **2009**, *48* (24), 4386–4389.

(20) Li, H.; Luo, L.; Kunal, P.; Bonifacio, C. S.; Duan, Z.; Yang, J. C.; Humphrey, S. M.; Crooks, R. M.; Henkelman, G. Oxygen Reduction Reaction on Classically Immiscible Bimetallics: A Case Study of RhAu. *J. Phys. Chem. C* **2018**, *122* (5), 2712–2716.

(21) Kulkarni, A.; Siahrostami, S.; Patel, A.; Nørskov, J. K. Understanding Catalytic

Activity Trends in the Oxygen Reduction Reaction. *Chem. Rev.* **2018**, *118* (5), 2302–2312.

(22) Schmid, G. Hexachlorododecakis(Triphenylphosphine)Pentapentacontagold, Au55(PPh3)12Cl6. *Inorg. Synth.* **1990**, *27*, 214–218.

(23) Boyen, H.; Kästle, G.; Koslowski, B.; Dietrich, C.; Ziemann, P.; Spatz, J. P.; Riethmüller, S.; Hartmann, C. Oxidation-Resistant Gold-55 Clusters. *Science.* **2002**, *297*, 1533–1536.

(24) Zhang, H.; Mautes, D.; Hartmann, U. A Study of Charge Quantization on Ligand-Stabilized Au55 Cluster Monolayers. *New J. Phys.* **2003**, *5*, 30.1-30.7.

(25) Wang, L.; Tang, Z.; Yan, W.; Yang, G.; Wang, Q.; Chen, S. Porous Carbon-Supported Gold Nanoparticles for Oxygen Reduction Reaction: Effects of Nanoparticle Size. *Appl. Mater. Interfaces* **2016**, *8*, 20635–20641.

(26) Tang, W.; Lin, H.; Kleiman-Shwarsctein, A.; Stucky, G. D.; McFarland, E. W. Size-Dependent Activity of Gold Nanoparticles for Oxygen Electroreduction in Alkaline Electrolyte. *J. Phys. Chem. C* **2008**, *112* (28), 10515–10519.

(27) Zhang, C.; Hwang, S. Y.; Peng, Z. Size-Dependent Oxygen Reduction Property of Octahedral Pt-Ni Nanoparticle Electrocatalysts. *J. Mater. Chem. A* **2014**, *2* (46), 19778–19787.

(28) Zhao, P.; Li, N.; Astruc, D. State of the Art in Gold Nanoparticle Synthesis. *Coord. Chem. Rev.* **2013**, *257* (3–4), 638–665.

(29) Lee, Y.; Loew, A.; Sun, S. Surface- and Structure-Dependent Catalytic Activity of Au Nanoparticles for Oxygen Reduction Reaction. *Chem. Mater.* **2010**, *22* (3), 755–761.

(30) Lu, L.; Lou, B.; Zou, S.; Kobayashi, H.; Liu, J.; Xiao, L.; Fan, J. Robust Removal of Ligands from Noble Metal Nanoparticles by Electrochemical Strategies. *ACS Catal.* **2018**, *8* (9), 8484–8492.

(31) Wu, L.; Xi, Z.; Sun, S. *Well-Defined Metal Nanoparticles for Electrocatalysis*, 1st ed.; Elsevier B.V., 2017.

(32) Pei, Y.; Shao, N.; Gao, Y.; Zeng, X. C. Investigating Active Site of Gold Nanoparticle Au55(PPh3)12Cl6 in Selective Oxidation. *ACS Nano* **2010**, *4* (4), 2009–2020.

(33) Schmid, G.; Klein, N.; Korste, L.; Kreibig, U.; Schönauer, D. Large Transition Metal Clusters-VI. Ligand Exchange Reactions on Au55(PPh3)12Cl6-the Formation of a Water Soluble Au55 Cluster. *Zeitschrift fur Naturforsch.* **1986**, *41b*, 1028–1032.

CHAPTER 2

(1) Schmid, G. The Relevance of Shape and Size of Au 55 Clusters. *Chem. Soc. Rev.* **2008**, *37* (9), 1909–1930.

(2) Ferrando, R.; Jellinek, J.; Johnston, R. L. Nanoalloys: From Theory to Applications of Alloy Clusters and Nanoparticles. *Chem. Rev.* **2008**, *108* (3), 845–910.

(3) Okamoto, H.; Massalski, T. B. The Au-Rh (Gold-Rhodium) System. **1984**, *5* (4), 384–387.

(4) Essinger-Hileman, E. R.; Decicco, D.; Bondi, J. F.; Schaak, R. E. Aqueous Room-Temperature Synthesis of Au-Rh, Au-Pt, Pt-Rh, and Pd-Rh Alloy Nanoparticles: Fully Tunable Compositions within the Miscibility Gaps. *J. Mater. Chem.* **2011**, *21* (31), 11599–11604.

(5) Luo, L.; Timoshenko, J.; Lapp, A. S.; Frenkel, A. I.; Crooks, R. M. Structural Characterization of Rh and RhAu Dendrimer-Encapsulated Nanoparticles. *Langmuir* **2017**, *33* (43), 12434–12442.

(6) García, S.; Anderson, R. M.; Celio, H.; Dahal, N.; Dolocan, A.; Zhou, J.; Humphrey, S. M. Microwave Synthesis of Au–Rh Core–Shell Nanoparticles and Implications of the Shell Thickness in Hydrogenation Catalysis. *Chem. Commun.* **2013**, *49* (39), 4241–4243.

(7) Li, H.; Luo, L.; Kunal, P.; Bonifacio, C. S.; Duan, Z.; Yang, J. C.; Humphrey, S. M.; Crooks, R. M.; Henkelman, G. Oxygen Reduction Reaction on Classically Immiscible Bimetallics: A Case Study of RhAu. *J. Phys. Chem. C* **2018**, *122* (5), 2712–2716.

(8) García, S.; Zhang, L.; Piburn, G. W.; Henkelman, G.; Humphrey, S. M. Microwave Synthesis of Classically Immiscible Rhodium-Silver and Rhodium-Gold Alloy Nanoparticles: Highly Active Hydrogenation Catalysts. *ACS Nano* **2014**, *8* (11), 11512–11521.

(9) Schmid, G. Hexachlorododecakis(Triphenylphosphine)Pentapentacontagold, Au55(PPh3)12Cl6. *Inorg. Synth.* **1990**, *27*, 214–218.

(10) Schmid, G.; Klein, N.; Korste, L.; Kreibig, U.; Schönauer, D. Large Transition Metal Clusters-VI. Ligand Exchange Reactions on Au55(PPh3)12Cl6-the Formation of a Water Soluble Au55 Cluster. *Zeitschrift fur Naturforsch.* **1986**, *41b*, 1028–1032.

(11) Genna, D. T.; Pfund, L. Y.; Samblanet, D. C.; Wong-Foy, A. G.; Matzger, A. J.; Sanford, M. S. Rhodium Hydrogenation Catalysts Supported in Metal Organic Frameworks: Influence of the Framework on Catalytic Activity and Selectivity. *ACS Catal.* **2016**, *6* (6), 3569–3574.

(12) Shih, K. C.; Goldman, A. S. Alkane Dehydrogenation Catalyzed by Rhodium(I) Phosphine Complexes: Observation of the Stoichiometric Alkane-to-Rhodium Hydrogen-Transfer Step. *Organometallics* **1993**, *12* (9), 3390–3392.

(13) Sparta, M.; Børve, K. J.; Jensen, V. R. Activity of Rhodium-Catalyzed Hydroformylation: Added Insight and Predictions from Theory. *J. Am. Chem. Soc.* **2007**, *129* (27), 8487–8499.

(14) Begum, A.; Bose, M.; Moula, G. Graphene Supported Rhodium Nanoparticles for Enhanced Electrocatalytic Hydrogen Evolution Reaction. *Sci. Rep.* **2019**, *9* (1), 1–10.

(15) Narouz, M. R.; Osten, K. M.; Unsworth, P. J.; Man, R. W. Y.; Salorinne, K.; Takano, S.; Tomihara, R.; Kaappa, S.; Malola, S.; Dinh, C. T.; et al. N-Heterocyclic Carbene-Functionalized Magic-Number Gold Nanoclusters. *Nat. Chem.* **2019**, *11* (5), 419–425.

(16) Schmid, G.; Pfeil, R.; Boese, R.; Bandermann, F.; Meyer, S.; Calis, G. H. M.; van der Velden, J. W. A. Au55[P(C6H5)3]12CI6 — Ein Goldcluster Ungewöhnlicher Größe. *Chem. Ber.* **1981**, *114*, 3634–3642.

(17) Duan, Z.; Timoshenko, J.; Kunal, P.; House, S. D.; Wan, H.; Jarvis, K.; Bonifacio, C.; Yang, J. C.; Crooks, R. M.; Frenkel, A. I.; et al. Structural Characterization of Heterogeneous RhAu Nanoparticles from a Microwave-Assisted Synthesis. *Nanoscale* **2018**, *10* (47), 22520–22532.

(18) Wang, G.; Xu, Y.; Qian, P.; Su, Y. ADP Potential for the Au-Rh System and Its Application in Element Segregation of Nanoparticles. *Comput. Mater. Sci.* **2021**, *186* (July 2020), 110002.

(19) Galyamova, A.; Shin, K.; Henkelman, G.; Crooks, R. M. Effect of TiOx Substrate Interactions on the Electrocatalytic Oxygen Reduction Reaction at Au

Nanoparticles. *J. Phys. Chem. C* **2020**, *124* (18), 10045–10056.

(20) Luo, J.; Wang, L.; Mott, D.; Njoki, P. N.; Kariuki, N.; Zhong, C. J.; He, T. Ternary Alloy Nanoparticles with Controllable Sizes and Composition and Electrocatalytic Activity. *J. Mater. Chem.* **2006**, *16* (17), 1665–1673.

(21) Nørskov, J. K.; Rossmeisl, J.; Logadottir, A.; Lindqvist, L.; Kitchin, J. R.; Bligaard, T.; Jónsson, H. Origin of the Overpotential for Oxygen Reduction at a Fuel-Cell Cathode. *J. Phys. Chem. B* **2004**, *108* (46), 17886–17892.

(22) Trindell, J. A.; Clausmeyer, J.; Crooks, R. M. Size Stability and H2/CO Selectivity for Au Nanoparticles during Electrocatalytic CO2 Reduction. *J. Am. Chem. Soc.* **2017**, *139* (45), 16161–16167.

(23) Braunstein, P.; Lehner, H.; Matt, D. A Platinum-Gold Cluster: Chloro-1κCl-Bis(Triethylphosphine-1κP)Bis(Triphenyl- Phosphine)-2κP, 3κP-Triangulo-Digold-Platinum(1 +) Trifluoromethanesulfonate. *Inorg. Synth.* **1990**, *27*, 218–221.

(24) Osborn, J. A.; Wilkinson, G. Tris(Triphenylphosphine)Halorhodium(I). *Inorg. Synth.* **1967**, *X*, 67–71.